Cytoplasmic Cl^- couples membrane remodeling to epithelial morphogenesis

Mu He[a], Wenlei Ye[a], Won-Jing Wang[d], Eirish S. Sison[a,c], Yuh Nung Jan[a,b,c], and Lily Yeh Jan[a,b,c,1]

[a]Department of Physiology, University of California, San Francisco, CA 94158; [b]Department of Biochemistry and Biophysics, University of California, San Francisco, CA 94158; [c]Howard Hughes Medical Institute, University of California, San Francisco, CA 94158; and [d]Institute of Biochemistry and Molecular Biology, College of Life Sciences, National Yang-Ming University, Taipei, 11221, Taiwan

Contributed by Lily Yeh Jan, November 18, 2017 (sent for review August 16, 2017; reviewed by Bingwei Lu and Blanche Schwappach)

Chloride is the major free anion in the extracellular space (>100 mM) and within the cytoplasm in eukaryotes (10 ~ 20 mM). Cytoplasmic Cl^- level is dynamically regulated by Cl^- channels and transporters. It is well established that movement of Cl^- across the cell membrane is coupled with cell excitability through changes in membrane potential and with water secretion. However, whether cytoplasmic Cl^- plays additional roles in animal development and tissue homeostasis is unknown. Here we use genetics, cell biological and pharmacological tools to demonstrate that TMEM16A, an evolutionarily conserved calcium-activated chloride channel (CaCC), regulates cytoplasmic Cl^- homeostasis and promotes plasma membrane remodeling required for mammalian epithelial morphogenesis. We demonstrate that TMEM16A-mediated control of cytoplasmic Cl^- regulates the organization of the major phosphoinositide species PtdIns(4,5)P_2 into microdomains on the plasma membrane, analogous to processes that cluster soluble and membrane proteins into phase-separated droplets. We further show that an adequate cytoplasmic Cl^- level is required for proper endocytic trafficking and membrane supply during early stages of ciliogenesis and adherens junction remodeling. Our study thus uncovers a critical function of CaCC-mediated cytoplasmic Cl^- homeostasis in controlling the organization of PtdIns(4,5)P_2 microdomains and membrane remodeling. This newly defined role of cytoplasmic Cl^- may shed light on the mechanisms of intracellular Cl^- signaling events crucial for regulating tissue architecture and organelle biogenesis during animal development.

calcium-activated chloride channel | epithelial morphogenesis | phosphoinositide | membrane remodeling | primary cilia

Ca^{2+}-activated Cl^- channel (CaCC), molecularly identified as TMEM16A (1–3), serves important functions in excitable cells. Activation of TMEM16A-CaCC in nociceptive dorsal root ganglion neurons generates Cl^- efflux, leading to membrane depolarization and action potential firing (4). TMEM16A-CaCC in the interstitial cells of Cajal plays a role in the generation of pacemaker activity in the stomach and intestines (5). TMEM16A-CaCC in the auditory inner supporting cells enhances the excitability of cochlear hair cells (6). In nonexcitable epithelial cells of the trachea, pancreas, mammary glands, and salivary glands, TMEM16A-CaCC is a major contributor of Cl^- secretion. For example, mucociliary transport in the airways depends on cholinergic Cl^- secretion mediated by TMEM16A (7, 8).

Intriguingly, genetic inactivation of TMEM16A in mice leads to perinatal lethality associated with early onset morphogenic defects in the tracheal and gastrointestinal tract (9). In the human genome, *TMEM16A* belongs to a group of 3,230 genes highly intolerant of loss-of-function mutations (10), indicating that TMEM16A is essential for human survival. Little is known, however, about the cellular mechanisms that underlie CaCC-dependent tissue formation during mammalian development.

In this study, we demonstrate that TMEM16A-CaCC is required for maintaining a critical level of cytoplasmic Cl^-. We further identified an unanticipated role of cytoplasmic Cl^- in regulating microdomain partitioning of PtdIns(4,5)P_2, also known simply as PI(4,5)P_2, one of the best-studied phosphoinositide (PI) species, on the plasma membrane (11), analogous to processes such as phase transition of membrane lipids (12). Paralleling changes in membrane phosphoinositide, intracellular Cl^- level can also modulate endocytic trafficking and recycling endosome to provide membrane supply during early stages of ciliogenesis and junction remodeling. We propose a model in which the fundamental role of TMEM16A in nonexcitable epithelial cells is to control the cytoplasmic Cl^- level, which serves a key regulatory mechanism for the maintenance of membrane phosphoinositide homeostasis and membrane remodeling, and may have profound impact on downstream signaling events. Given that epithelial tissues constitute essential barriers and perform critical physiological functions in almost all major organs, our study provides important mechanistic insight into how Cl^- channels contribute to tissue architecture and function.

Results

Consistent with a high level of TMEM16A expression in epithelial cells (13–15), *Tmem16a* mutant embryos exhibited abnormalities in the pseudostratified tracheal epithelium and cuboidal kidney tubules with complete penetrance (Fig. 1 *A*–*C*). In particular, compared with wild-type littermates, *Tmem16a*$^{-/-}$ mutants had epithelial organs with enlarged lumens. Using whole-cell patch-clamp recording, we confirmed the deficiency of CaCC activity in *Tmem16a*$^{-/-}$ mouse embryonic fibroblasts (Fig. S1*A*). In mouse trachea, en face examination of the apical cell borders with phalloidin and tight junction marker ZO-1 staining revealed a change of cell packing. In the control trachea, the epithelium underwent a transition from pentagons at E14.5 to hexagons at E18.5 (Fig. 1 *D* and *E*). This transition from

Significance

Calcium-activated chloride channels (CaCCs) serve important physiological functions, including modulation of signal processing of neurons in the central and peripheral nervous system. In this study, we uncover a previously underappreciated role for TMEM16A, an evolutionarily conserved CaCC, in regulating cytoplasmic chloride homeostasis and membrane remodeling events in nonexcitable epithelial tissues. TMEM16A-mediated intracellular chloride homeostasis can modulate the partitioning of membrane phosphoinositides and endocytic transport, providing a new mechanism that controls membrane dynamics, a key property of eukaryotic cell membranes important for numerous cellular processes in development and diseases.

Author contributions: M.H., Y.N.J., and L.Y.J. designed research; M.H., W.Y., W.-J.W., and E.S.S. performed research; M.H., W.Y., and W.-J.W. analyzed data; and M.H., Y.N.J., and L.Y.J. wrote the paper.

Reviewers: B.L., Stanford University School of Medicine; and B.S., Institute of Molecular Biology, Universitätsmedizin Göttingen.

The authors declare no conflict of interest.

[1]To whom correspondence should be addressed. Email: Lily.Jan@ucsf.edu.

This article contains supporting information online at www.pnas.org/lookup/suppl/doi:10.1073/pnas.1714448115/-/DCSupplemental.

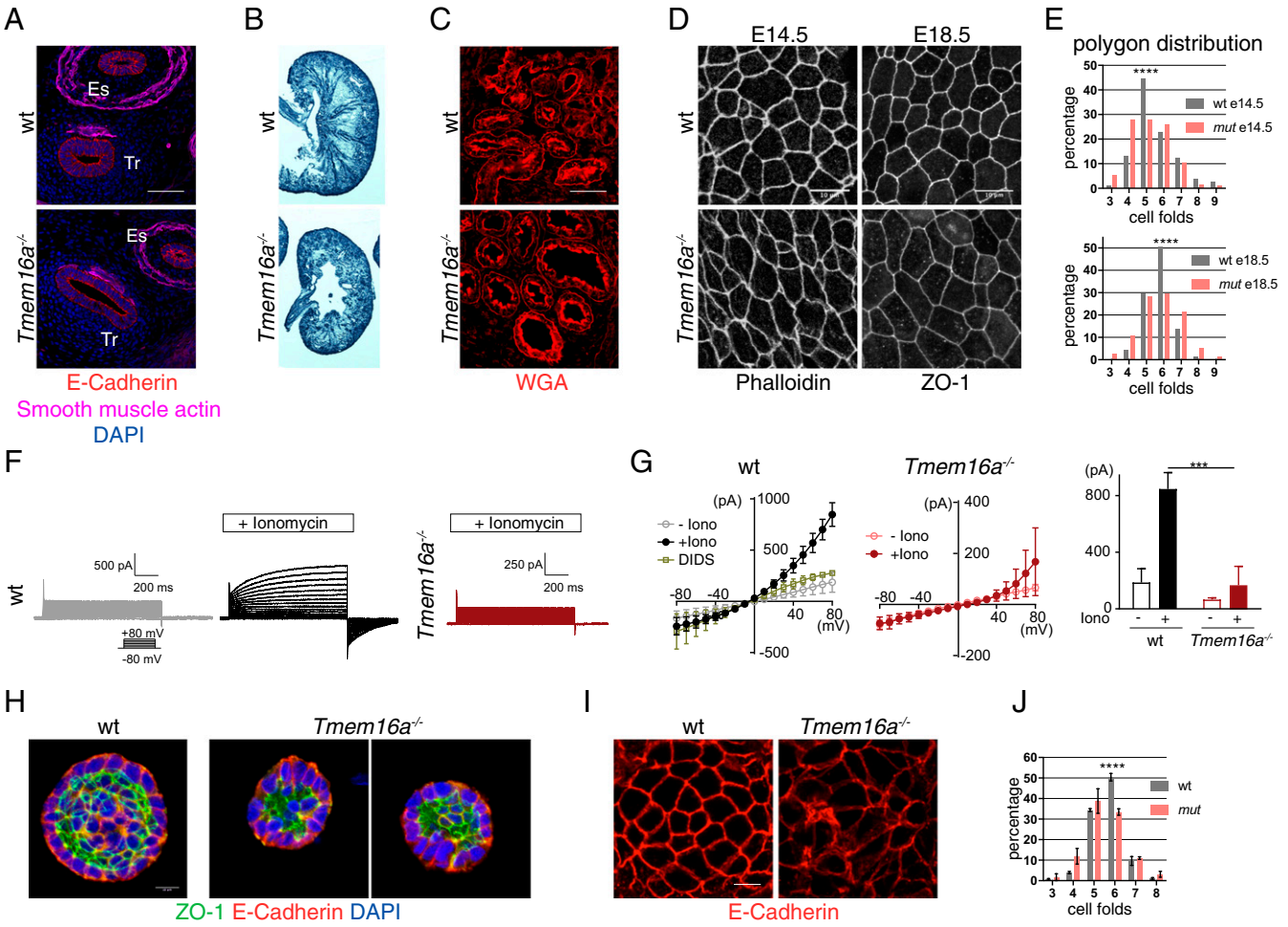

Fig. 1. Epithelium organization defects in the absence of TMEM16A. (*A*) Sections of E13.5 trachea and esophagus and (*B*) hematoxylin staining of E18.5 whole kidneys from control and *Tmem16a* mutant embryos. E-cadherin marks cell membrane. Smooth-muscle actin marks smooth muscle ($n = 3$ for each genotype at each time point). (*C*) Collecting tubules stained with wheat germ agglutinin (WGA) in control and *Tmem16a* mutant embryos. (Scale bar, 20 μm.) (*D*) En face view of the apical surface of embryonic day 14.5 (E14.5) and E18.5 trachea and (*E*) quantifications of cell folds. Cell borders were marked with phalloidin. For E14.5, 186 control cells and 204 mutant cells, from three embryos of each genotype, were pooled, respectively, for analysis ($n = 3$). For E18.5, 380 control cells and 389 mutant cells, from four embryos for each genotype, were pooled, respectively, for analysis. (Scale bar, 10 μm.) $^{****}P <$ 0.0001 with two-tailed unpaired *t* test ($n = 4$). (*F* and *G*) Whole-cell recording of CaCC in control and *Tmem16a* KO embryonic fibroblasts ($n = 5$ cells for each genotype were recorded). $^{***}P < 0.001$ with two-tailed unpaired *t* test. (*H*) Spheroids formed by control and *Tmem16a* KO mIMCD3 cells in 3D Matrigel. ZO-1 labels apical tight junction. E-cadherin labels cell membrane, and DAPI labels nucleus. (Scale bar, 20 μm.) (*I*) Zoomed apical organization of control and *Tmem16a* KO mIMCD3 spheroids. (*J*) Cell shape analysis using E-cadherin as cell membrane marker. A total of 150 cells from control or mutant spheroids, respectively, were analyzed ($n = 3$). Bar indicates SEM. $^{****}P < 0.0001$ with two-tailed unpaired *t* test.

dynamic epithelia to stable epithelia was severely impaired in *Tmem16a*$^{-/-}$ mutants (Fig. 1 *D* and *E*). The development of specific packing geometries of the epithelium is tightly regulated by a combination of cell junction dynamics and the rate of proliferation (16, 17). As proliferation is not disrupted by the removal of TMEM16A (9), our data indicate that TMEM16A plays a role in promoting cell junction remodeling to achieve optimal cell packing during epithelial morphogenesis.

To characterize cellular function of TMEM16A, we developed an *in vitro* cell model using mouse inner medullary collecting duct cells (mIMCD3) that is amenable to pharmacological treatment with CaCC blockers (Fig. S1*B*). We further generated two independent *Tmem16a* KO mIMCD3 cell lines using CRISPR-mediated gene editing (Fig. S1*C*). Whole-cell patch-clamp recording confirmed the absence of CaCC in *Tmem16a* KO mIMCD3 cells (Fig. 1 *F* and *G*). When cultured in 3D Matrigel, mIMCD3 cells can self-organize into polarized spheroids that resemble their *in vivo* architectures (18). In contrast to control mIMCD3 cells that formed organized spheroids with clear lumens, both *Tmem16a* KO mIMCD3 cell lines formed much smaller spheroids with disorganized lumens, although overall polarity appeared normal (Fig. 1*H*). Polygon distribution in *Tmem16a* KO spheroids showed fewer hexagonal cells compared with control (Fig. 1 *I* and *J*). Treatment of control cells with benzbromarone, a specific TMEM16A channel blocker (7), resulted in spheroids with abnormal lumen morphology similar to those formed by *Tmem16a* KO cells (Fig. S1*B*). Thus, genetic inactivation and pharmacological inhibition of TMEM16A-CaCC all led to abnormal spheroid architecture, suggesting that CaCC channel activity is important for epithelial morphogenesis.

When expressed in kidney epithelial cell lines, TMEM16A-GFP was present on the plasma membrane, as well as on membrane protrusions such as the microvilli stained by phalloidin (Fig. 2*A*). Given the primary function of TMEM16A is to permeate chloride across the plasma membrane, we determined whether TMEM16A activity can alter the cytoplasmic Cl^- level in mIMCD3 cells using live imaging and a fluorescently encoded Cl^- sensor as a readout for intracellular Cl^- concentration (19)

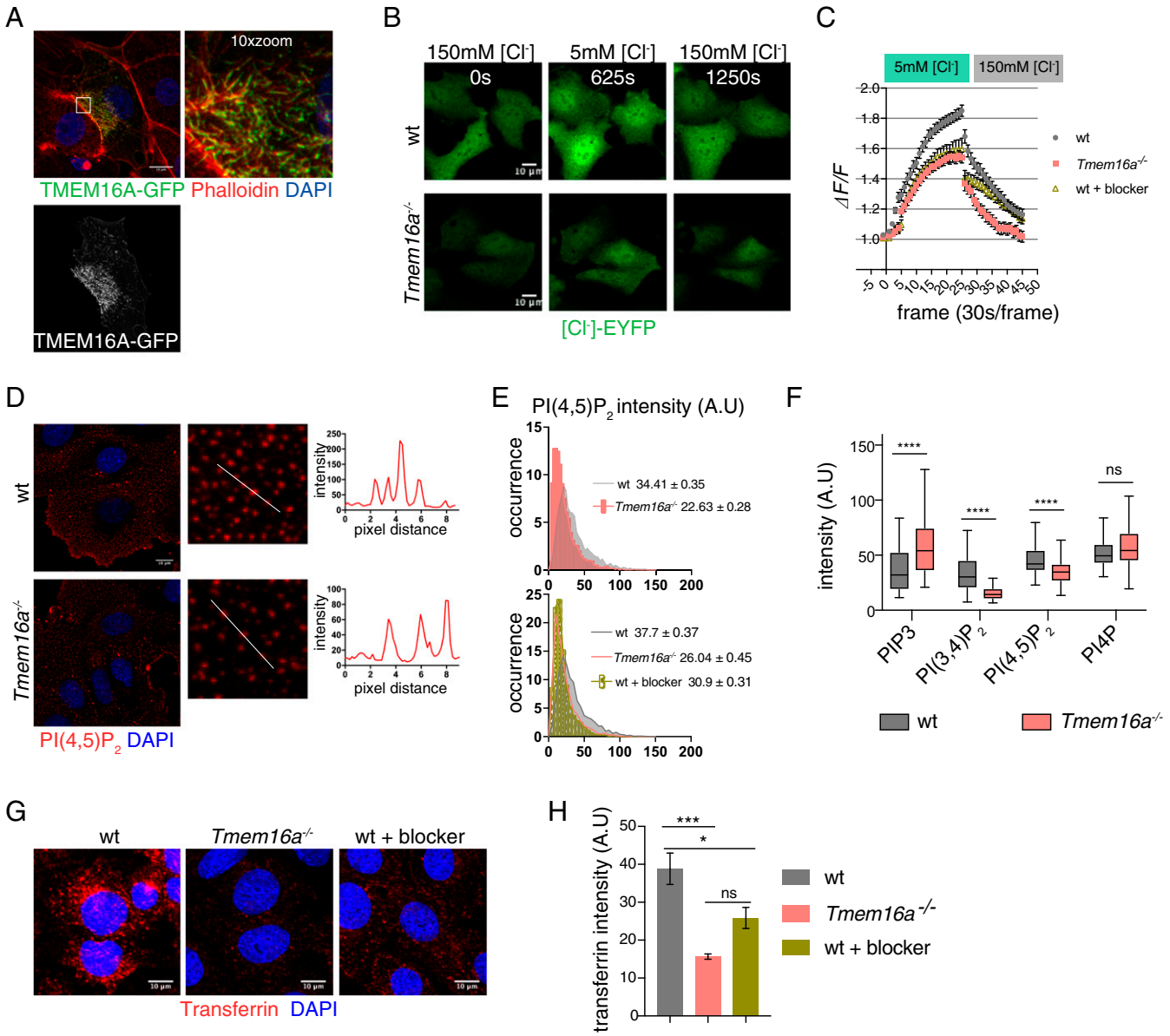

Fig. 2. TMEM16A-CaCC regulates the formation of PtdIns(4,5)P_2 microdomains and transferrin endocytosis. (*A*) Phalloidin labels F-actin and microvilli. DAPI labels nucleus. (Scale bars, 10 μm.) (*B*) Snapshots of [Cl^-]-EYFP sensor expressed in control and *Tmem16a*$^{-/-}$ cells. (Scale bar, 10 μm.) (*C*) Changes in Cl^- YFP sensor intensity in control, *Tmem16a* mutants and 20 μM benzbromarone-treated control cells. A total of 40–50 cells for each condition were pooled for analyses. Bar represents SEM ($n = 3$). (*D*) Immunostaining of PtdIns(4,5)P_2 in control and *Tmem16a* KO cells. (*E*) Profile of PtdIns(4,5)P_2 microdomains in control, *Tmem16a* KO cells and blocker-treated control cells. Mean for each genotype is indicated ± SEM; ****$P < 0.0001$ with two-tailed unpaired *t* test ($n = 3$); ****$P < 0.0001$ with χ^2 test for frequency distribution. Fifty cells were measured for each condition. A.U = arbitrary unit. (*F*) Fluorescence intensity of membrane PIs in control and *Tmem16a* KO cells. A total of 80–100 cells were analyzed for each genotype and each lipid marker. ****$P < 0.0001$ using two-tailed Mann–Whitney test. ns = not significant. Results are presented as Tukey plots ($n = 3$), including outliers. (*G*) Transferrin uptake in control, *Tmem16a* KO cells, and blocker-treated control cells. (*H*) Quantification of internal transferrin shown in *G*. Sixty cells pooled from three independent experiments were analyzed. $P < 0.0001$ by one-way ANOVA. ***$P = 0.0004$, *$P = 0.0173$, ns, not significant. Bar represents SEM.

(Fig. 2 *B* and *C*). As the fluorescence intensity of Cl^- sensor is inversely related to the intracellular Cl^- concentration, an increase in sensor fluorescence intensity correlates with Cl^- efflux and a reduction of the cytoplasmic Cl^- level. Bathing in low Cl^- solution (5 mM Cl^- and 145 mM gluconate, a large anion impermeable to Cl^- channels and transporters) resulted in an increase of the Cl^- sensor fluorescence intensity by 1.85 ± 0.24 fold in control cells, significantly higher than the 1.60 ± 0.31 fold increase in control cells treated with CaCC blocker, and the 1.54 ± 0.20 fold increase in *Tmem16a* KO cells (Fig. 2*C*). The difference of Cl^- sensor intensity change between control and mutant cells may reflect the contribution of TMEM16A-mediated Cl^- efflux, supporting a role of TMEM16A in epithelial cells for controlling intracellular Cl^- homeostasis.

Given the membrane localization of TMEM16A and its ability to modulate cytoplasmic Cl^- concentration, we further characterized the cellular defects in *Tmem16a* mutants and looked for alterations in signaling molecules that might account for the *Tmem16a* mutant phenotypes. We began by examining phosphoinositides (PIs) (Fig. S2*A*), which are central regulators in many aspects of the endo/exocytosis pathways in controlling tissue organization and function (11, 20–24). Among the major

PIs on the plasma membrane, PtdIns(4,5)P_2 plays an essential role in clathrin-mediated endocytosis and is mostly enriched on the plasma membrane (20). A semiquantitative assessment of PtdIns(4,5)P_2 staining on the plasma membrane (25) revealed that in control cells, PtdIns(4,5)P_2 was present in a punctate pattern (Fig. 2 *D* and *E*), consistent with the presence of membrane PtdIns(4,5)P_2 microdomains (12). The intensity of PtdIns(4,5)P_2 microdomains was reduced in *Tmem16a* KO cells and in control cells treated with the CaCC blocker benzbromarone (Fig. 2*E*). Those PtdIns(4,5)P_2 microdomains were sensitive to membrane 5′ lipid phosphatase (26), as recruitment of INPP5E to the plasma membrane strongly diminished the intensity of PtdIns(4,5)P_2 microdomains in control cells (Fig. S2*B*). The data indicate that TMEM16A-CaCC channel activity contributes to the heterogeneous membrane composition and partitioning of PtdIns(4,5)P_2 microdomains of variable sizes. The amount of plasma membrane PIP_3 and PtdIns(3,4)P_2 were also misregulated in *Tmem16a* KO cells (Fig. 2*F*), indicating a general role of TMEM16A-CaCC in regulating phosphoinositides homeostasis.

We next determined whether TMEM16A plays a role in modulating receptor-mediated endocytosis, which depends on the membrane PtdIns(4,5)P_2 activity. Both control and *Tmem16a* KO cells were incubated with Alexa Fluor 594-conjugated transferrin (Trf) at 4 °C for 30 min to allow saturated binding and to prevent internalization of surface-bound Trf; unbound Trf was subsequently removed by washing with cold media. After incubation at 37 °C for 30 min, the intensity of internalized Trf in *Tmem16a* KO cells was about 40% of that in control cells (Fig. 2 *G* and *H*). With treatment of the CaCC blocker benzbromarone during the internalization period, Trf uptake in wild-type cells was about 67% of that in control cells without blocker treatment (Fig. 2 *G* and *H*).

In control cells, the localization of internalized Trf strongly overlapped with that of Rab11A-GFP, a molecular signature that defines the juxtanuclear endosomal recycling compartment (ERC) and slow recycling endosomes (27, 28), and of pericentrin, a protein that marks the centrosome and adjacent centrosomal materials. In *Tmem16a* KO cells, the amount of Trf colocalized with either Rab11A-GFP or pericentrin was reduced, and Trf appeared to be more diffuse within the cell (Fig. S2*C*). Thus, the lack of TMEM16A impairs Trf accumulation at the ERC near the centrosome, which may reflect the decrease of total Trf internalization in *Tmem16a* KO cells.

In light of the ability of inactivation of TMEM16A-CaCC to impair the levels of membrane PIs and Trf uptake, we asked whether intracellular Cl^- dynamics was linked to membrane PIs and Trf endocytosis. Assessed by membrane PtdIns(4,5)P_2 immunostaining, mIMCD3 cells cultured in low Cl^- solution for 45 min showed redistribution of the PtdIns(4,5)P_2 microdomains and induced the formation of large PtdIns(4,5)P_2 positive tubular/ring-like structures near the cell periphery (Fig. 3 *A* and *B* and Fig. S3*A*), similar to the uncoated endocytic structures during massive endocytosis or macropinocytosis (29). To determine whether changes in PtdIns(4,5)P_2 in cells exposed to low Cl^- and high gluconate were due to changes in the membrane potential, we replaced 145 mM gluconate with 145 mM I^-, which permeates most Cl^- channels including TMEM16A (30, 31) and thus might alter the membrane potential differently from gluconate. High I^- treatment similarly induced dimmer PtdIns(4,5)P_2 microdomains and large PtdIns(4,5)P_2 positive tubular structures (Fig. 3*A* and Fig. S3*A*). Using a previously characterized $PH_{PLC}\delta$ domain tagged to GFP (PH-GFP) (32, 33) to visualize PtdIns(4,5)P_2, we characterized the dynamics of PtdIns(4,5)P_2 during Cl^- efflux by live imaging. Low Cl^- treatment induced extensive ruffling around the cell periphery as well as PH-GFP positive structures on the membrane (Fig. 3*C*). Those structures were highly dynamic, forming and disappearing, but became more stable toward the end of the 45-min imaging period. The data suggest that the reduction in the intracellular Cl^- concentration may account for changes in membrane PtdIns(4,5)P_2.

Low Cl^- treatment for 45 min reduced Trf fluorescence intensity within the cells bathed in either gluconate or I^- compared with cells cultured in control solution, but caused a strong accumulation of Trf colocalized with Rab11A-GFP at the ERC, as well as Trf-positive and Rab11-GFP positive vesicles at cell periphery (Fig. 3 *D* and *E*). Analyses of the kinetics of internalized Trf in response to Cl^- efflux revealed that lowering intracellular Cl^- can promote recycling endosome accumulation at the ERC (Fig. 3*F*) and alter the time course of Trf receptor recycling back to the plasma membrane (Fig. 3*E*).

E-cadherin endocytosis and recycling are particularly important mechanisms for cell junction remodeling. Given the effect of Cl^- efflux on Trf endocytosis, we determined whether low cytoplasmic Cl^- could trigger E-cadherin internalization. In a preconfluent mIMCD3 monolayer, E-cadherin was mostly present on the cell membrane at the cell–cell contacts, colocalized with F-actin. Treatment of low Cl^- solution containing either 145 mM gluconate or 145 mM I^- induced formation of ruffled cell–cell contacts and internalization of E-cadherin into small vesicles. F-actin also became more diffuse and less concentrated on the cell–cell contacts (Fig. 3*G*). Thus, paralleling the changes in membrane PtdIns(4,5)P_2, low Cl^- also induced abnormal accumulation of Trf at the ERC as well as internalization of E-cadherin; the similar effects of high gluconate or high I^- on E-cadherin and Trf recycling can be accounted for by alteration of cytoplasmic Cl^- controlled by CaCC rather than channels on the recycling endosomal membrane. The effect of low Cl^- on Trf trafficking and E-cadherin dynamics was reversible, as incubation of normal Cl^- solution facilitated Trf clearing from the ERC in cells pretreated with low Cl^- solution, and caused internalized E-cadherin to be reinserted to the junctions and the disappearance of ruffled cell–cell contacts (Fig. S3 *B* and *C*). Thus, the effects on Trf endocytosis and E-cadherin dynamics involving recycling endosomes are specific to low Cl^- and reversible by restoring normal Cl^- concentration.

Changes in membrane PI homeostasis and membrane remodeling in the absence of TMEM16A-CaCC may also affect organelles on the plasma membrane. We asked whether TMEM16A-CaCC–dependent membrane remodeling is required for the formation of cilia (Fig. S4*A*), which are key signaling and sensory organelles present on the apical surface in most if not all epithelial cells. Treatment of CaCC blocker at different times during spheroid formation demonstrated that the activity of TMEM16A-CaCC was particularly important at the initiation stage for both cilium and lumen formation (Fig. S4 *B*–*D*). Consistent with the finding that vesiculotubular structures are enriched at the pericentrosomal area at the onset of ciliogenesis but not after cilia formation (23, 24, 34), our data are in agreement with the report that TMEM16A-CaCC blockers affect ciliogenesis of cultured epithelial cells (35). We next examined the morphology of primary cilia in wild-type and *Tmem16a* null mouse embryos by using the cilia marker Arl13b, a small GTPase specifically localized to the ciliary membrane (36). Various epithelial cell types in the kidney, pancreas, and trachea exhibited significantly shorter primary cilia in *Tmem16a*$^{-/-}$ mutant embryos compared with those in littermate controls (Fig. 4*A* and Fig. S4*A*). En face imaging of E14.5 trachea by scanning electron microscopy confirmed that primary cilia were shorter in *Tmem16a* mutants, and fewer cilia were observed in mutants than in controls (Fig. 4*B*). By estimation the ratio of cell surface to cilia surface is close to 400 (37). If a perturbation of endocytosis was sufficient to affect primary cilia elongation in cells lacking TMEM16A, we wondered whether such perturbation in membrane supply would lead to more severe defects in cells that form a large number of motile cilia. Immunofluorescence (IF) staining with acetylated α-tubulin and scanning electron microscopy revealed that motile cilia were less dense and appeared shorter in the mutant trachea at embryonic day 18.5 (E18.5), as if they had not fully emerged (Fig. 4

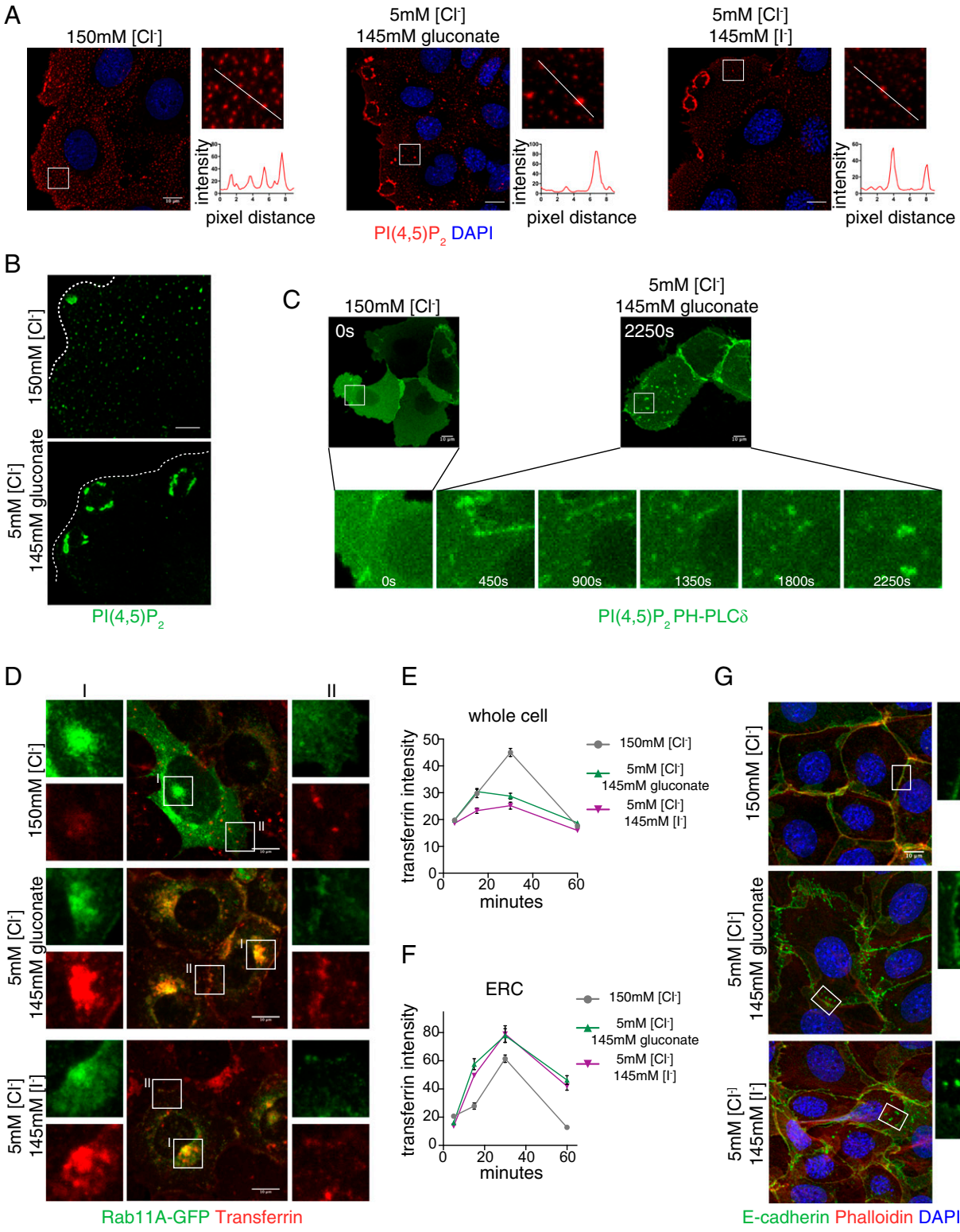

Fig. 3. Efflux of cytoplasmic Cl^- affects membrane PtdIns(4,5)P_2 distribution and impairs transferrin recycling. (*A*) Immunostaining of PtdIns(4,5)P_2 in control and low Cl^--treated mIMCD3 cells. (*B*) Zoomed images of PtdIns(4,5)P_2 staining in control and low Cl^--treated mIMCD3 cells. Dashed lines outline cell borders. (*C*) Expression of $PH_{PLC}\delta$-GFP in mIMCD3 cells treated with control and low Cl^- solution. Snapshots of $PH_{PLC}\delta$-GFP during Cl^- efflux at indicated time points. (*D*) Rab11-GFP and transferrin in control and low Cl^--treated mIMCD3 cells. Enlarged *Insets* show transferrin at the ERC (*I*) or cell periphery (*II*). (*E*) Total internal transferrin intensity quantified at 5, 15, 30, and 60 min of internalization. (*F*) Transferrin at the ERC quantified at 5, 15, 30, and 60 min of internalization. Sixty cells were measured for each condition from three independent experiments. (*G*) E-cadherin and F-actin, labeled by phalloidin in control and low Cl^--treated mIMCD3 cells. (Scale bars, 10 μm.)

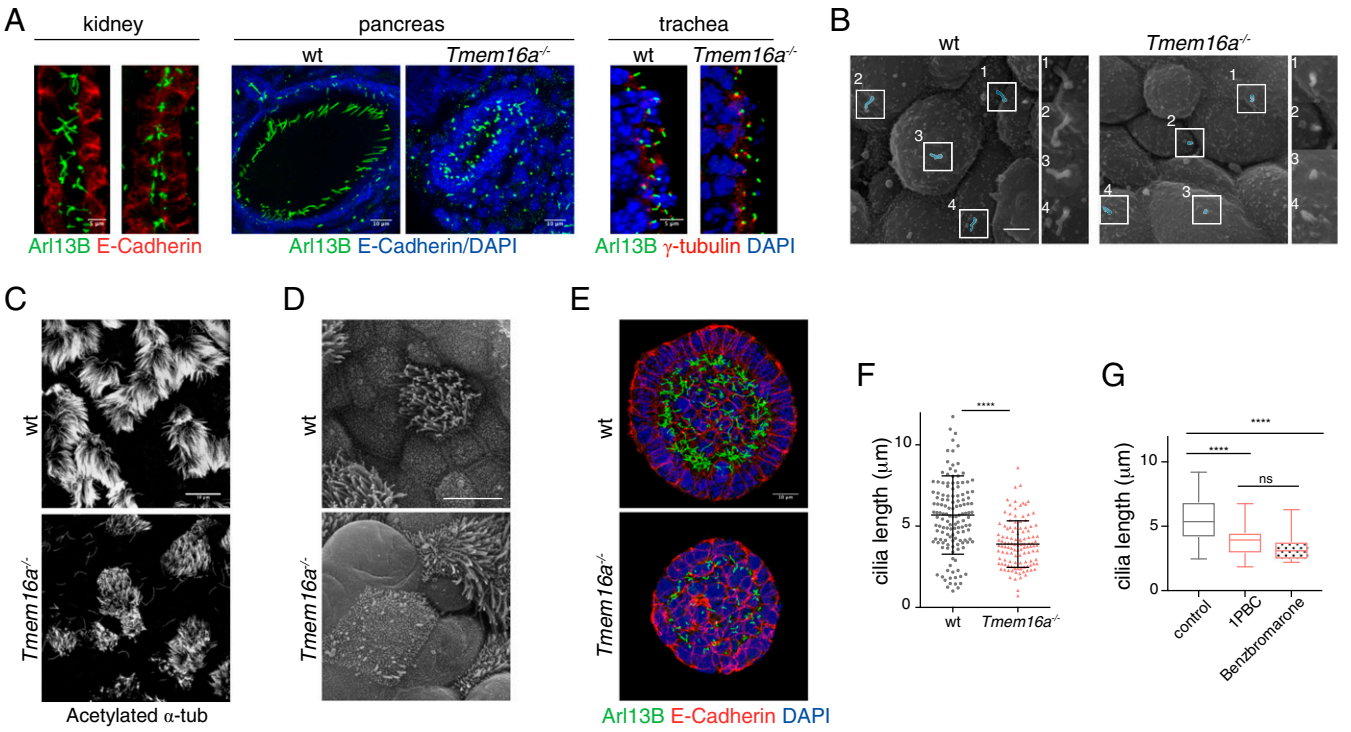

Fig. 4. TMEM16A-CaCC is required for proper cilia elongation. (*A*) Sections of kidney tubules, pancreatic ducts, and trachea of control and *Tmem16a*$^{-/-}$ embryos. Arl13b labels primary cilia. E-cadherin labels basal lateral cell membrane. γ-Tubulin labels basal body. DAPI labels nuclei. (Scale bars, 5 μm.) (*B*) Scanning electron micrographs of control and *Tmem16a*$^{-/-}$ mutant trachea. Primary cilia are highlighted. (Scale bar, 2.5 μm.) (*C*) Tracheal motile cilia stained with acetylated α-tubulin at E18.5 and P0 from control and *Tmem16a*$^{-/-}$ mutant embryos. (Scale bar, 10 μm.) (*D*) En face scanning electron micrographs of tracheal motile cilia from P0 control and *Tmem16a* mutants. (Scale bar, 20 μm.) (*E*) Spheroids formed by control and *Tmem16a* KO mIMCD3 cells in 3D Matrigel. Arl13b labels cilia. E-cadherin labels cell membrane, and DAPI labels nucleus. (Scale bar, 10 μm.) (*F*) Length measurements of cilia in control and *Tmem16a* KO mIMCD3 cells using Arl13b as a cilia marker. A total of 139 control cilia and 119 mutant cilia were pooled from four independent experiments. ****$P < 0.0001$ with two-tailed Welch's *t* test and all data were plotted. Error bar represents SD. (*G*) Cilia length in control mIMCD3 cells treated with two TMEM16A-CaCC blockers measured with Arl13b staining as a cilia marker. ****$P < 0.0001$ by one-way ANOVA; ns, not significant. Plots represent 10–90% of cilia length distribution. Fifty cells from each treatment were pooled from three independent experiments.

C and *D*). Thus, in the absence of TMEM16A, motile cilia extension was impaired in the trachea epithelium. Consistent with the defects seen in *Tmem16a*$^{-/-}$ mutant embryos, primary cilia were much shorter in *Tmem16a* KO cell lines as well as in control mIMCD3 cells treated with benzbromarone and 1PBC (Fig. 4 *E*–*G*). Thus, genetic inactivation and pharmacological inhibition of TMEM16A-CaCC all led to shortened cilia, highlighting a critical role of TMEM16A-CaCC in providing membrane supply during early stages of ciliogenesis.

Given the effect of low Cl^- on membrane PtdIns(4,5)P_2, Trf trafficking, and E-cadherin dynamics, we next determined whether modulation of cytoplasmic Cl^- could reverse tissue and cellular defects of *Tmem16a* mutants. When *Tmem16a* KO cells were incubated in 75 mM Cl^-, the intensity of PtdIns(4,5)P_2 microdomains was significantly increased compared with those mutant cells cultured in 150 mM Cl^- (Fig. 5*A*). Further, exposure of *Tmem16a* KO cells to 75 mM extracellular Cl^- induced Trf accumulation to the ERC (Fig. 5 *B* and *C*). Thus, reduction in the Cl^- level in *Tmem16a* KO cells can increase Trf uptake and recruit more recycling endosomes to the ERC, thereby partially rescuing mutant phenotypes.

We further tested whether this partial restoration of endocytosis and membrane PIP_2 may rescue defects of ciliogenesis and tissue architecture in 3D matrigel culture. mIMCD3 cells cultured in 150 mM or 75 mM Cl^- formed cilia with comparable length. The diameter of control spheroids in 75 mM Cl^- was smaller compared with spheroids cultured in 150 mM Cl^-. *Tmem16a* KO cells, when cultured in 75 mM Cl^- media, formed primary cilia significantly longer than those of mutant cells cultured in 150 mM Cl^-, and the diameter of *Tmem16a* KO spheroids exhibited a 20% increase (Fig. 5 *D* and *E* and Fig. S4 *E* and *F*). When cultured in media with 75 mM Cl^- for 4 d, *Tmem16a* KO spheroids contained more hexagonally shaped cells, compared with the pentagonally packed spheroids cultured in normal media with 150 mM Cl^- (Fig. 5*F*). Consistent with the finding that low Cl^- promotes E-cadherin internalization and that E-cadherin turnover at the cell–cell junctions promotes epithelial cell rearrangement, the cell packing defects observed in *Tmem16a* mutant embryos and *Tmem16a* KO cells could arise from a reduction in E-cadherin turnover due to compromised Cl^- homeostasis. To determine whether TMEM16A-dependent epithelial morphogenesis is primarily mediated through phosphoinositol signaling, we next assessed whether depletion of PIP_2 can exacerbate the cellular defects in *Tmem16a* mutants. At a micromolar concentration, wortmannin, a nonselective PI3K inhibitor, can also inhibit PI4K activity, which is required for PIP_2 replenishment (38, 39). When incubated with 25 μM wortmannin for 12 h, control spheroids appeared similar to those incubated with regular culture media. In treated spheroids, tight junctions, marked by ZO-1, localized normally to the apical surface of the lumen, while primary cilia, marked by Arl13b, showed comparable morphology and density (Fig. S5). In contrast, wortmannin-treated *Tmem16a* KO spheroids exhibited collapsed lumen and ectopic localization of ZO-1 to the basal–lateral membrane. In the presence of wortmannin, the fluorescent intensity of Arl13b appeared diffuse, indicating a stronger structural defect associated with the primary cilia (Fig. S5).

Discussion

Our findings uncover an unanticipated role of mammalian TMEM16A-CaCC in controlling membrane remodeling important

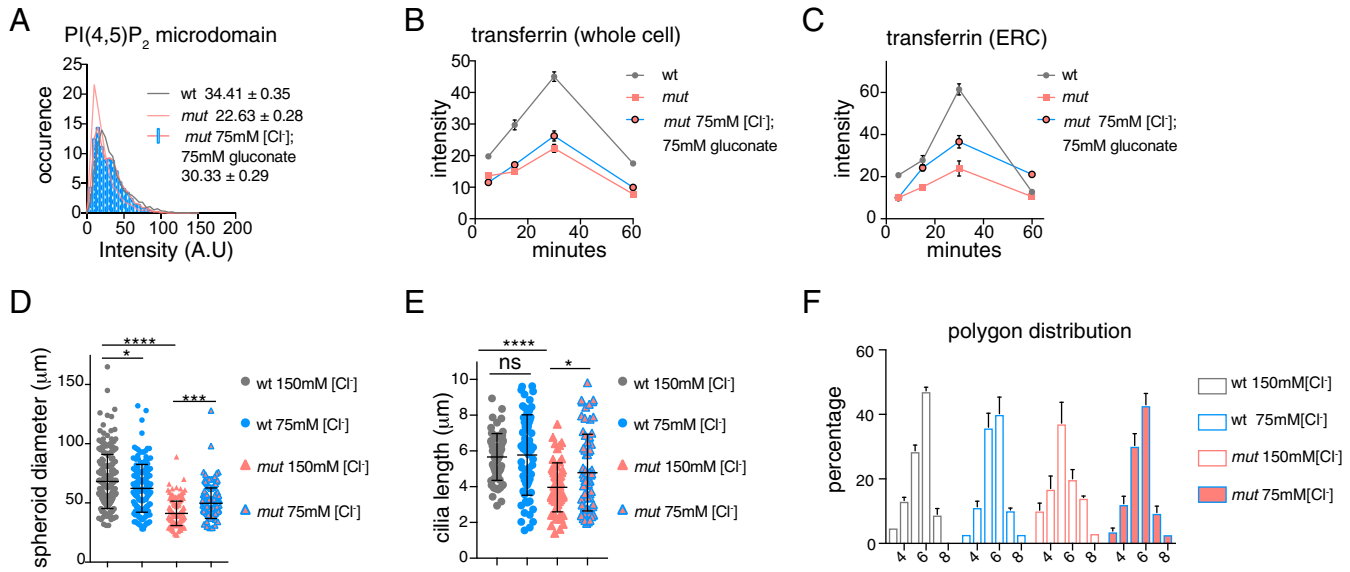

Fig. 5. Modulations of cytoplasmic Cl^- concentration affect ciliogenesis and epithelial organization. (*A*) Profile of PtdIns(4,5)P_2 microdomains in control, *Tmem16a* mutants, and mutants treated with 75 mM Cl^- solution. Mean for each genotype is indicated ± SEM; ****$P < 0.0001$ with two-tailed unpaired *t* test ($n = 3$); ****$P < 0.0001$ with χ^2 test for frequency distribution. Fifty cells were measured for each condition. (*B*) Whole-cell internalized Trf intensity and (*C*) ERC Trf intensity quantified at 5, 15, 30, and 60 min of internalization. Fifty cells for each condition were pooled from three independent experiments. (*D*) Measurements of lumen size using prominin. *$P < 0.05$; ***$P < 0.001$; ****$P < 0.0001$ by one-way ANOVA. More than 200 cells were measured for each condition from three independent experiments. (*E*) Measurements of cilia length using Arl13b. *$P < 0.05$; ****$P < 0.0001$ by one-way ANOVA. A total of 250 cilia were measured for each condition from three independent experiments. Error bars in *D* and *E* represent SD. (*F*) Cell shape analysis using E-cadherin as cell membrane marker. A total of 150 cells from five spheroids were analyzed from three independent experiments. Error bar indicates SEM.

for epithelial morphogenesis at both tissue and organelle levels. Consistent with a crucial role in regulating epithelial organization and ciliogenesis, the morphological defects of *Tmem16a*$^{-/-}$ mutants share common features with known human congenital disorders. For example, esophageal and tracheal abnormalities associated with TMEM16A inactivation are identical to those seen in *Ift172*^{avc1}, a mouse model for ciliopathy and human vertebral anomalies (V), anal atresia (A), tracheoesophageal fistulas (TE), and renal (R) and limb (L) anomalies, collectively called the VACTERL association (40). The tubular atrophy and cysts seen in *Tmem16a*$^{-/-}$ mutant kidneys are markedly similar to those of nephronophthisis, a rare inheritable human kidney disease that primarily affects children (41).

Our data suggest that the activity of TMEM16A-CaCC in regulating epithelial morphogenesis depends on its chloride permeation to modulate membrane phosphoinositide distribution and promotes endocytic trafficking, which controls apical membrane delivery and adherens junction turnover. Because changes of intracellular Cl^- level can modulate the organization of PtdIns(4,5)P_2 microdomains and transferrin recycling, and partially rescue *Tmem16a* mutant defects, our data suggest that the function of TMEM16A in tissue morphogenesis depends on its ability to permeate Cl^- ions to maintain the cytoplasmic Cl^- homeostasis. Within the cell, an optimal cytoplasmic Cl^- level may provide an important regulatory mechanism for proper phosphoinositide functions and many critical downstream signaling events conducive for the formation of a stable epithelium.

Given that electrostatic interactions are sufficient to organize PtdIns(4,5)P_2 and its interacting proteins into microdomains, it is possible that cytoplasmic Cl^- provides an ideal electrostatic environment that favors the formation of PtdIns(4,5)P_2 microdomains and interactions among PtdIns(4,5)P_2 binding partners (12, 42). Alternatively, it is possible that Cl^- may directly interact with enzymes that metabolize phospholipids or GTP-binding proteins such as ARF6 that can activate PIP5K to promote local PIP2 production (32). With Cl^- as the predominant anion, enzymes may have evolved to form association with Cl^-, which in turn can fine tune enzymatic output. Our discovery of the role of cytoplasmic Cl^- homeostasis in epithelial morphogenesis and development underscores the importance of examining possible underlying mechanisms in future studies.

Materials and Methods

Mice. The *Tmem16a* null allele, Ano1^{tm1Jrr}, has been described previously (9). Breeding colonies were maintained in a mixed genetic background by outcrossing C57BL/6J Ano1^{tm1Jrr} males to FVB females, which were obtained from The Jackson Laboratory. Mice were housed in an animal facility and maintained in a temperature-controlled and light-controlled environment with an alternating 12-h light/dark cycle. A maximum of five mice were housed per cage. All protocols have been approved by the University of California San Francisco Institutional Animal Care and Use Committee.

Cell Cultures and Generation of TMEM16A Knockout mIMCD3 Cells. Primary mouse embryonic fibroblasts (MEFs) were derived from E10.5 mouse embryos using standard protocols, as previously described (43). mIMCD3 cells were obtained from American Type Culture Collection (ATCC). Only cells under 15 passages from the parental ATCC stock were used for analyses. MEFs were grown in DMEM (Gibco) supplemented with 10% bovine calf serum, penicillin, and streptomycin. To induce cilia formation, confluent MEFs and NIH 3T3 cultures were serum starved for 24 h. mIMCD3 cells were cultured in DMEM/F12 1:1 (Gibco), supplemented with 10% bovine calf serum, penicillin, and streptomycin.

To generate CRISPR-mediated knockout of TMEM16A, a guide DNA oligo dimer (5′ GCATACTTGCATTCGGCGTCG 3′) targeted to exon 3 of mouse *Tmem16a* was inserted into the vector pSpCas9(BB)-2A-Puro (PX459) V2.0 (Addgene 62988) as described (44). One day after seeding, mIMCD3 cells at ~70% confluence were transfected with the Tmem16a-PX459 plasmid using Lipofectamine 3000 (Invitrogen) according to the manufacturer's instructions. Two days posttransfection, cells were incubated with fresh media plus 1 μg/mL puromycin (Sigma) for 3–5 d. Nontransfected cells were used as control to determine the killing dose and time for puromycin selection. Individual puromycin-resistant clones were isolated with cloning cylinders (Sigma) and expanded in normal media. For genotyping, genomic DNA was isolated from clone and control cells using the quick DNA purification protocol from The Jackson Laboratory. A 300-bp fragment including exon 3 was amplified and cloned into pcR4-TOPO TA vector (Invitrogen), which was transformed into Dh5α competent *Escherichia coli* (New England Biolabs). From each transformation, 8–10 bacteria colonies were analyzed to determine the sites of mutations via sequencing.

Antibodies, Constructs, and Immunostaining. Antibodies for immunofluorescence staining were rabbit anti-Arl13b (36) (1:2,000 dilution), mouse anti-acetylated α-tubulin (1:2,000; 6–11B-1; Sigma-Aldrich T6793), mouse anti–γ-tubulin (1:2,000; GTU-88; Sigma-Aldrich T6557), rat anti–E-cadherin (1:1,000; ECCD-2; Thermo Fisher Scientific), mouse anti-CD133 (1:500; 13A4; Millipore), mouse anti-pericentrin (1:500; 30/pericentrin; BD Biosciences), mouse anti-ZO1 (1:1,000; ZO1-1A12; Thermo Fisher Scientific), mouse anti-PI(4)P (1:250; Z-P004; Echelon Biosciences), mouse anti-PI(4,5)P_2 (1:250; Z-A045; Echelon Biosciences), mouse anti-PI(3,4)P_2 (1:150; Z-P034b; Echelon Biosciences), mouse anti-PIP_3 (1:300; Z-P345; Echelon Biosciences), wheat germ agglutinin (1:2,000; Alexa Fluor 568 conjugate; Thermo Fisher Scientific), phalloidin (1:250: Alexa Fluor 488 conjugate; Thermo Fisher Scientific), and Alexa Fluor 488-, 594- and 633-conjugated secondary antibodies (Invitrogen). mEmerald-RAB11A-7 plasmid was donated by the Michael Davidson laboratory at the Florida State University, Florida, USA. and obtained from the Nikon Imaging Center at the University of California, San Francisco. Membrane-tethered mRFP-FKBP-INPP5E and Lyn_{11}-FRB-CFP were obtained from Addgene. Benzbromarone (Tocris Bioscience) and wortmannin (Sigma) were reconstituted with DMSO.

For protein immunostaining, cells or tissue sections were fixed with 2% paraformaldehyde (PFA) for 20 min at room temperature; for centrosomal markers, samples were treated with cold methanol for 5 min after PFA fixation. Immunostaining of cells and sections was carried out as described (43). Briefly, after fixation, samples were washed and blocked with IF buffer (1× PBS with 1% heat-inactivated goat/donkey serum and 0.3% Triton X-100). Primary antibodies were added and incubated for 1 h at room temperature or overnight at 4 °C. After washing with IF buffer, secondary antibodies and DAPI were added at 1:1,000 dilution for 1 h at room temperature. Samples were washed with 1× PBS and mounted with Fluoromount-G (SouthernBiotech). Lipid staining was performed as described (25, 26). Briefly, cells were fixed with 4% paraformaldehyde and 0.2% glutaraldehyde and permeabilized with 0.3% saponin instead of Triton X-100. Washing and staining were performed with IF buffer (1× PBS with 5% serum and 0.2% saponin) at room temperature. Samples were then imaged using a Leica TCS SP5 or SP8 confocal microscope with the 63× HC PL Apo oil CS2 objective.

Transferrin Uptake Assay. Control and *Tmem16a* KO mIMCD3 cells, either nontransfected or mEmerald-Rab11A transfected using Lipofectamine 3000, were seeded on gelatin-coated coverslips. The second day, cells were serum starved for 2 h and used for transferrin uptake as described (45). Briefly, cells were incubated with 25 μg/mL transferrin (Alexa Fluor 594 conjugate, Thermo Fisher Scientific) diluted in normal serum-free DMEM/F12 at 4 °C. After being washed three times with ice-cold DMEM/F12, cells were incubated with phenol red-free media or Tyrode's solution (145 mM NaCl, 5 mM KCl, 10 mM Hepes, 2 mM $CaCl_2$, 1 mM $MgCl_2$, 10 mM glucose, pH 7.3 adjusted with NaOH, 290 Osmol/L) with 5% serum at 37 °C to allow transferrin uptake. Coverslips were fixed at specific time points with 4% paraformaldehyde, and processed for confocal imaging using a Leica SP8. To induce Cl^- efflux, cells were incubated with low Cl^- Tyrode's solution (145 mM Na gluconate, 5 mM KCl, 10 mM Hepes, 2 mM $CaCl_2$, 1 mM $MgCl_2$, 10 mM glucose, pH 7.3, 299 Osmol/L) or high I^- Tyrode's solution (145 mM NaI, 5 mM KCl, 10 mM Hepes, 2 mM $CaCl_2$, 1 mM $MgCl_2$, 10 mM glucose, pH 7.3, 290 Osmol/L).

Chloride Sensor Confocal Live Imaging. Control and *Tmem16a* KO mIMCD3 cells were transfected with EYFP plasmids (19) using Lipofectamine 3000 and seeded onto gelatin-coated 35-mm glass bottom dishes. On the day of imaging, cells were washed with PBS and switched to normal Tyrode's solution with 5% serum and equilibrated for 10 min at 37 °C. To induce Cl^- efflux, cells were switched to low Cl^- Tyrode's solution with 5% serum. To induce Cl^- influx, low Cl^- solution was removed and normal Tyrode's solution was added back. Live imaging was performed using a Leica SP8 confocal microscope with the 40× HC PL Apo oil CS2 objective in a temperature- and CO_2-controlled chamber. Cells were imaged for 20 min at 30 s per frame. Movies and snapshots were generated using Fiji/ImageJ.

Scanning Electron Microscopy. For scanning electron microscope, embryonic and newborn tracheas were dissected in cold PBS and fixed with 2% paraformaldehyde and 2.5% glutaraldehyde in 0.1 M sodium cacodylate buffer. After buffer rinses, samples were postfixed in 1% OsO_4 at room temperature for 4 h followed by dehydrating in an ethanol series. Critical point drying was done with a Hitachi HCP-2 critical point dryer. Samples were coated with a Hitachi E-1010 ion sputter. An FEI Quanta 200 scanning electron microscope at 20 kV was used for viewing and imaging.

Whole-Cell Recording. Standard Tyrode's solution (145 mM NaCl, 5 mM KCl, 10 mM Hepes, 2 mM $CaCl_2$, 1 mM $MgCl_2$, 10 mM glucose, pH 7.3 adjusted with NaOH, 290 Osmol/L) was used for whole-cell recording. The pipette solution contained 150 mM *N*-methyl-D-glucamine (NMDG)-Cl, 10 mM Hepes, 0.5 mM EGTA, pH 7.3–7.4 (adjusted with HCl). For recording, cells were lifted from their culture dishes with 0.05% trypsin-EDTA and plated onto coverslips. After cells settled for about 20 min, coverslips were transferred to a recording chamber on a Nikon-TE2000 inverted scope. Whole-cell patch-clamp recordings were performed using borosilicate capillary glass electrodes (Sutter Instrument) polished to a tip resistance of 2–3 MΩ. Data were collected with an Axopatch 700B patch-clamp amplifier and a Digidata 1440 digitizer with pClamp10 software (Molecular Devices). I–V curves were graphed with Origin 6 (OriginLab).

Spheroid Formation. mIMCD3 spheroids were cultured as described (18). Either 20 μM benzbromarone or 10 μM 1PBC was added to DMEM/F12 media for the CaCC blocker treatment. Spheroids were cultured with fresh media plus 10% serum, with or without blocker, for 4–5 d, and fixed with 4% paraformaldehyde. Immunostaining and image acquisition were described above.

Imaging Analysis. The fluorescence intensity of proteins and lipids were analyzed using line-scan based analysis in Fiji/ImageJ. Either raw data or normalized intensity were presented. For analysis of transferrin uptake, cells with either perinuclear or cytoplasmic transferrin localization were counted. For each measurement, cell area was outlined with the freehand selection tool in Fiji/ImageJ and the average intensity per pixel of transferrin was used for quantification. Alternatively, if a cell junction marker was used, such as phalloidin, cell area was defined by the pattern of apical phalloidin. The internalized transferrin at different time points was normalized to the average amount of transferrin internalized at the first time point (5 min postinternalization); the fold change in transferrin intensity was used to distinguish between uptake and recycling defects.

For analysis of PIP_2 microdomains, a 10-pixel wide and 200-pixel long straight line was drawn using the line tool of Fiji/ImageJ near the cell periphery of randomly selected cells to generate the intensity profile of PIP_2 microdomains. The intensity of PIP_2 microdomains was plotted by frequency distribution analysis using Prism. Quantification of plasma membrane lipids was performed using the same approach as transferrin internalization analysis.

For cell neighbor and polygon analysis, cell shapes were determined by phalloidin, ZO-1, or E-cadherin staining. The numbers of edges per cell were determined by Neighbor Analysis in the BioVoxxel Toolbox in Fiji/ImageJ or manually, from at least three embryonic samples or 10 spheroids per genotype. Data analysis was performed with Excel and Prism7.

Statistical Analysis. Methods for statistical analysis and numbers of samples measured in this study are specified in the figure legends. The error bars indicate the SEM or box and whisker plot from 10 to 90% or Tukey plot.

ACKNOWLEDGMENTS. We thank Kathryn Anderson (Sloan Kettering Institute) for providing the Arl13b antibody, Wann-Neng Jane (Institute of Plant and Microbial Biology, Academia Sinica) for assistance with scanning electron microscopy sample preparation and image acquisition, Joseph Santos-Sacchi and Sheng Zhong for the YFP chloride sensor, Peng Jin for critical reading of the manuscript, and members of the L.Y.J. laboratory for discussion. This work is supported by NIH Grants (R01NS069229 to L.Y.J. and F32HD089639 to M.H.). L.Y.J. and Y.N.J. are investigators of the Howard Hughes Medical Institute.

1. Yang YD, et al. (2008) TMEM16A confers receptor-activated calcium-dependent chloride conductance. *Nature* 455:1210–1215.
2. Schroeder BC, Cheng T, Jan YN, Jan LY (2008) Expression cloning of TMEM16A as a calcium-activated chloride channel subunit. *Cell* 134:1019–1029.
3. Caputo A, et al. (2008) TMEM16A, a membrane protein associated with calcium-dependent chloride channel activity. *Science* 322:590–594.
4. Cho H, et al. (2012) The calcium-activated chloride channel anoctamin 1 acts as a heat sensor in nociceptive neurons. *Nat Neurosci* 15:1015–1021.
5. Hwang SJ, et al. (2009) Expression of anoctamin 1/TMEM16A by interstitial cells of Cajal is fundamental for slow wave activity in gastrointestinal muscles. *J Physiol* 587: 4887–4904.
6. Wang HC, et al. (2015) Spontaneous activity of cochlear hair cells triggered by fluid secretion mechanism in adjacent support cells. *Cell* 163:1348–1359.
7. Huang F, et al. (2012) Calcium-activated chloride channel TMEM16A modulates mucin secretion and airway smooth muscle contraction. *Proc Natl Acad Sci USA* 109: 16354–16359.
8. Ousingsawat J, et al. (2009) Loss of TMEM16A causes a defect in epithelial Ca2+-dependent chloride transport. *J Biol Chem* 284:28698–28703.
9. Rock JR, Futtner CR, Harfe BD (2008) The transmembrane protein TMEM16A is required for normal development of the murine trachea. *Dev Biol* 321:141–149.
10. Lek M, et al.; Exome Aggregation Consortium (2016) Analysis of protein-coding genetic variation in 60,706 humans. *Nature* 536:285–291.

11. Balla T (2013) Phosphoinositides: Tiny lipids with giant impact on cell regulation. *Physiol Rev* 93:1019–1137.
12. van den Bogaart G, et al. (2011) Membrane protein sequestering by ionic protein-lipid interactions. *Nature* 479:552–555.
13. Faria D, et al. (2014) The calcium-activated chloride channel Anoctamin 1 contributes to the regulation of renal function. *Kidney Int* 85:1369–1381.
14. Huang F, et al. (2009) Studies on expression and function of the TMEM16A calcium-activated chloride channel. *Proc Natl Acad Sci USA* 106:21413–21418.
15. Rock JR, Harfe BD (2008) Expression of TMEM16 paralogs during murine embryogenesis. *Dev Dyn* 237:2566–2574.
16. Farhadifar R, Röper J-C, Aigouy B, Eaton S, Jülicher F (2007) The influence of cell mechanics, cell-cell interactions, and proliferation on epithelial packing. *Curr Biol* 17: 2095–2104.
17. Gibson WT, Gibson MC (2009) Cell topology, geometry, and morphogenesis in proliferating epithelia. *Curr Top Dev Biol* 89:87–114.
18. Giles RH, Ajzenberg H, Jackson PK (2014) 3D spheroid model of mIMCD3 cells for studying ciliopathies and renal epithelial disorders. *Nat Protoc* 9:2725–2731.
19. Zhong S, Navaratnam D, Santos-Sacchi J (2014) A genetically-encoded YFP sensor with enhanced chloride sensitivity, photostability and reduced ph interference demonstrates augmented transmembrane chloride movement by gerbil prestin (SLC26a5). *PLoS One* 9:e99095.
20. Posor Y, Eichhorn-Grünig M, Haucke V (2015) Phosphoinositides in endocytosis. *Biochim Biophys Acta* 1851:794–804.
21. Martín-Belmonte F, et al. (2007) PTEN-mediated apical segregation of phosphoinositides controls epithelial morphogenesis through Cdc42. *Cell* 128:383–397.
22. Shewan A, Eastburn DJ, Mostov K (2011) Phosphoinositides in cell architecture. *Cold Spring Harb Perspect Biol* 3:a004796.
23. Sung C-H, Leroux MR (2013) The roles of evolutionarily conserved functional modules in cilia-related trafficking. *Nat Cell Biol* 15:1387–1397.
24. Pedersen LB, Mogensen JB, Christensen ST (2016) Endocytic control of cellular signaling at the primary cilium. *Trends Biochem Sci* 41:784–797.
25. Hammond GRV, Schiavo G, Irvine RF (2009) Immunocytochemical techniques reveal multiple, distinct cellular pools of PtdIns4P and PtdIns(4,5)P(2). *Biochem J* 422:23–35.
26. Hammond GRV, et al. (2012) PI4P and PI(4,5)P2 are essential but independent lipid determinants of membrane identity. *Science* 337:727–730.
27. Grant BD, Donaldson JG (2009) Pathways and mechanisms of endocytic recycling. *Nat Rev Mol Cell Biol* 10:597–608.
28. Mayor S, Parton RG, Donaldson JG (2014) Clathrin-independent pathways of endocytosis. *Cold Spring Harb Perspect Biol* 6:a016758.
29. Kirkham M, et al. (2005) Ultrastructural identification of uncoated caveolin-independent early endocytic vehicles. *J Cell Biol* 168:465–476.
30. Jentsch TJ, Stein V, Weinreich F, Zdebik AA (2002) Molecular structure and physiological function of chloride channels. *Physiol Rev* 82:503–568.
31. Duran C, Thompson CH, Xiao Q, Hartzell HC (2010) Chloride channels: Often enigmatic, rarely predictable. *Annu Rev Physiol* 72:95–121.
32. Brown FD, Rozelle AL, Yin HL, Balla T, Donaldson JG (2001) Phosphatidylinositol 4,5-bisphosphate and Arf6-regulated membrane traffic. *J Cell Biol* 154:1007–1017.
33. Hammond GRV, Balla T (2015) Polyphosphoinositide binding domains: Key to inositol lipid biology. *Biochim Biophys Acta* 1851:746–758.
34. Kim J, et al. (2010) Functional genomic screen for modulators of ciliogenesis and cilium length. *Nature* 464:1048–1051.
35. Ruppersburg CC, Hartzell HC (2014) The Ca2+-activated Cl- channel ANO1/TMEM16A regulates primary ciliogenesis. *Mol Biol Cell* 25:1793–1807.
36. Caspary T, Larkins CE, Anderson KV (2007) The graded response to sonic hedgehog depends on cilia architecture. *Dev Cell* 12:767–778.
37. Nachury MV (2014) How do cilia organize signalling cascades? *Philos Trans R Soc Lond B Biol Sci* 369:20130465.
38. Bain J, et al. (2007) The selectivity of protein kinase inhibitors: A further update. *Biochem J* 408:297–315.
39. Suh B-C, Hille B (2002) Recovery from muscarinic modulation of M current channels requires phosphatidylinositol 4,5-bisphosphate synthesis. *Neuron* 35:507–520.
40. Friedland-Little JM, et al. (2011) A novel murine allele of intraflagellar transport protein 172 causes a syndrome including VACTERL-like features with hydrocephalus. *Hum Mol Genet* 20:3725–3737.
41. Hildebrandt F, Attanasio M, Otto E (2009) Nephronophthisis: Disease mechanisms of a ciliopathy. *J Am Soc Nephrol* 20:23–35.
42. Brown DA (2015) PIP2Clustering: From model membranes to cells. *Chem Phys Lipids* 192:33–40.
43. He M, et al. (2014) The kinesin-4 protein Kif7 regulates mammalian hedgehog signalling by organizing the cilium tip compartment. *Nat Cell Biol* 16:663–672.
44. Ran FA, et al. (2013) Genome engineering using the CRISPR-Cas9 system. *Nat Protoc* 8: 2281–2308.
45. Reineke JB, Xie S, Naslavsky N, Caplan S (2015) Qualitative and quantitative analysis of endocytic recycling. *Sorting and Recycling Endosomes*, Methods in Cell Biology (Elsevier, Amsterdam), pp 139–155.